Vortex motion of dust particles due to non-conservative ion drag force in a plasma

Kil-Byoung Chai and Paul M. Bellan

Articles you may be interested in

Bulk ion acceleration and particle heating during magnetic reconnection in a laboratory plasmaa)
Phys. Plasmas **21**, 055706 (2014); 10.1063/1.4874331

Propagation and oblique collision of ion-acoustic solitary waves in a magnetized dusty electronegative plasma
Phys. Plasmas **20**, 122114 (2013); 10.1063/1.4853555

Three dimensional dust-acoustic solitary waves in an electron depleted dusty plasma with two-superthermal ion-temperature
Phys. Plasmas **20**, 013707 (2013); 10.1063/1.4789620

Tripolar vortex formation in dense quantum plasma with ion-temperature-gradients
Phys. Plasmas **19**, 052303 (2012); 10.1063/1.4714648

On the higher-order solution of the dust-acoustic solitary waves in a warm magnetized dusty plasma with dust charge variation
Phys. Plasmas **11**, 3303 (2004); 10.1063/1.1739235

Vortex motion of dust particles due to non-conservative ion drag force in a plasma

Kil-Byoung Chai[a)] and Paul M. Bellan[b)]

Applied Physics and Materials Science, Caltech, Pasadena, California 91125, USA

Vortex motion of the dust in a dusty plasma is shown to result because non-parallelism of the ion density gradient and the gradient of the magnitude of the ion ambipolar velocity cause the ion drag force on dust grains to be non-conservative. Dust grain poloidal vortices consistent with the model predictions are experimentally observed, and the vortices change character with imposed changes in the ion temperature profile as predicted. For a certain ion temperature profile, two adjacent co-rotating poloidal vortices have a well-defined X-point analogous to the X-point in magnetic reconnection. © 2016 AIP Publishing LLC. [http://dx.doi.org/10.1063/1.4941973]

I. INTRODUCTION

Dusty plasmas, a composition of electrons, ions, charged dust particles, and neutrals reproduce at macroscopic scales many intriguing phenomena that only occur at microscopic scales in conventional media. Examples include formation of crystal structure,[1] solid-liquid phase transitions,[2] kinetic-level dynamics in fluids,[3] and viscous heating.[4] Dust particle vortex flow has attracted much recent attention because of relevance to waves, instabilities, and turbulent transport.[5,6] Dust particle vortex flow has been observed in microgravity experiments,[7,8] in experiments where the gravitational force is compensated by the thermophoretic force,[9,10] and in experiments where the vortex flow is externally induced by a probe or by a laser.[11,12] However, the cause of vortex flows remains controversial. Akdim and Goedheer[13] and Schwabe and Graves[14] postulated that a non-zero curl of the total force exerted on dust particles causes vortex flow; Shimizu *et al.*[10] argued that dust particle vortex flow is induced by vortex neutral gas flow caused by the temperature gradient between two electrodes; and Fortov *et al.*[15] claimed that dust particle vortex flow results when the gradient of dust charge is not parallel to non-electrostatic forces such as the ion drag force and gravitational force.

Vortex streamlines are topologically similar to magnetic fields and, in particular, the poloidal magnetic field in tokamaks, spheromaks, and reversed field pinches have a vortex-like structure.[16,17] Magnetic field lines do not break or reconnect in ideal magnetohydrodynamics but if resistivity is non-zero, the magnetic field can break and reconnect.[18,19] Such magnetic reconnection is ubiquitous in both laboratory and space plasmas.[20,21] Vortices can also be ideal (zero viscosity, no reconnection) or non-ideal (finite viscosity, reconnection).

The Caltech water-ice dusty plasma experiment was constructed for studying nucleation, growth, and dynamics of water-ice grains formed in a plasma environment with liquid nitrogen-cooled background gas.[22] We have observed several interesting phenomena, namely, (i) spontaneous nucleation of water-ice grains in the plasma when water vapor is injected,[22] (ii) nonspherical growth of these water-ice grains under certain conditions,[22,23] and (iii) alignment of elongated ice grains.[23] We have also observed vortex flows of the ice dust grains. Recently, after aluminum heat shields were installed around the electrodes to lower the temperature, significant changes were observed in the vortex flow pattern. In order to explain these observations, we propose here a dust vortex formation model. This model predicts that dust particle vortex flow is driven by a torque resulting from the non-conservative nature of the ion drag force exerted on a dust particle. Our model predicts the observed axisymmetric vortex flows for typical density and temperature profiles of a dusty plasma experiment both with and without the heat shields.

II. MODEL

Figure 1 shows a sketch of our experiment with coordinate system indicated. Because of the azimuthal symmetry the model numerical calculations will show the $\{r, z\}$ plane and so correspond to the dashed line box in Fig. 1(b); video files which are presented later additionally show the region to the left of the z axis in Fig. 1.

The momentum equation for electrons or ions in a steady-state non-equilibrium plasma is given by[24]

$$n_\sigma q_\sigma \mathbf{E} - \nabla P_\sigma - \nu_{\sigma n} n_\sigma m_\sigma \mathbf{u}_\sigma = 0. \qquad (1)$$

By assuming the plasma is isothermal so $\nabla P_\sigma = k_B T_\sigma \nabla n_\sigma$, Eq. (1) can be recast as an equation for the flux $\Gamma_\sigma = n_\sigma \mathbf{u}_\sigma$ of escaping particles where
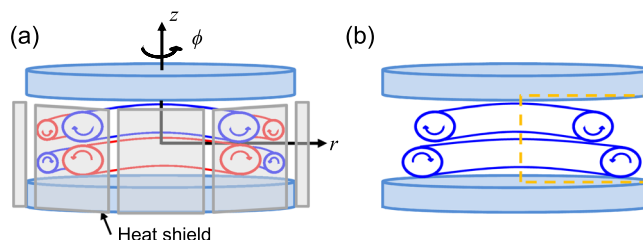

FIG. 1. Sketch of our system (a) with and (b) without heat shield. Axisymmetric vortices are observed from experiment and the flow directions are indicated as arrows.

a)kbchai@caltech.edu
b)pbellan@caltech.edu

$$\Gamma_\sigma = \pm\mu_\sigma n_\sigma \mathbf{E} - D_\sigma \nabla n_\sigma. \tag{2}$$

Here, $\mu_\sigma = |q_\sigma|/m_\sigma \nu_{\sigma n}$ is the mobility and $D_\sigma = k_B T_\sigma/m_\sigma \nu_{\sigma n}$ is the diffusion coefficient. The dust particles do not escape from the plasma so $\Gamma_d = 0$.

Because the electrons are lighter than ions, electrons escape the plasma more readily so the remaining plasma has a positive potential with respect to the chamber walls and electrodes. Thus, an ambipolar electric field develops to balance the electron and ion fluxes so

$$\mu_i n_i \mathbf{E} - D_i \nabla n_i = -\mu_e n_e \mathbf{E} - D_e \nabla n_e. \tag{3}$$

Charge neutrality gives $n_i = n_e + Z_d n_d$ where Z_d is the number of charges carried by a dust particle. With $\alpha = Z_d n_d/n_i$ the ambipolar electric field becomes

$$\mathbf{E} = \frac{D_i \nabla n_i - D_e \nabla n_e}{\mu_i n_i + \mu_e n_e} = \frac{D_i \nabla n_i - D_e \nabla n_i + D_e \nabla (n_d Z_d)}{\mu_i n_i + \mu_e n_i (1-\alpha)}. \tag{4}$$

We assume α is small in order to obtain an approximate analytic solution that reveals the essential physical process and therefore we can say, that $\nabla(n_d Z_d) = \alpha \nabla n_i \ll \nabla n_i$; the assumption that α is small will be validated in Sec. V. Since $T_e \gg T_i$ (so that $D_e \gg D_i$) and $\mu_e \gg \mu_i$, Eq. (4) reduces to

$$\mathbf{E} \simeq -\frac{D_e \nabla n_i}{\mu_e n_i (1-\alpha)}. \tag{5}$$

The ion flux can then be expressed as

$$\Gamma_i = \frac{-k_B T_e \nabla n_i}{m_i \nu_{in}(1-\alpha)} - D_i \nabla n_i \simeq -\frac{T_e D_i}{T_i(1-\alpha)} \nabla n_i$$
$$= -\frac{D_a}{(1-\alpha)} \nabla n_i, \tag{6}$$

where $D_a = T_e D_i/T_i$ is the ambipolar diffusion coefficient that would exist if there were no dust particles.

In a steady-state bulk plasma where ionization dominates recombination the ion continuity equation reduces to $\nabla \cdot \Gamma_i = G$ where $G = \nu_{iz} n_e$ is the ionization source term and $\nu_{iz} = K_{iz0} \exp(-E_{iz}/k_B T_e) n_g$ [24] is the ionization rate. Substituting for Γ_i using Eq. (6) and using $n_e = (1-\alpha)n_i$ the ion continuity equation becomes

$$\frac{1}{r}\frac{\partial}{\partial r}\left(r\frac{\partial n_i}{\partial r}\right) + \frac{\partial^2 n_i}{\partial z^2} + \frac{\nu_{iz}}{D_{a0}} n_i (1-\alpha)^2 = 0. \tag{7}$$

With small α, the solution to Eq. (7) is $n_i(r,z) = n_{i0} J_0(\chi_{01}r/R)\cos(\pi z/L)$ with $\nu_{iz}/D_{a0} = \chi_{01}^2/R^2 + \pi^2/L^2$; here, n_{i0} is the ion density at the origin, R is the electrode radius, L is the gap between the electrodes, and χ_{01} is the first zero of the Bessel function $J_0(s)$. Contours of u_i and n_i/n_{i0} determined in Eqs. (6) and (7) are shown in Fig. 2(a) as dashed and solid lines, respectively, using parameters $R = 2.7$ cm, $L = 1.4$ cm, $T_i = 0.015$ eV, and $P_{Ar} = 200$ mTorr; these parameters correspond to the experiment to be discussed.

Electrostatic, ion drag, neutral drag, thermophoretic, and gravitational forces are typically exerted on dust particles in a plasma. The electrostatic force is caused by the interaction
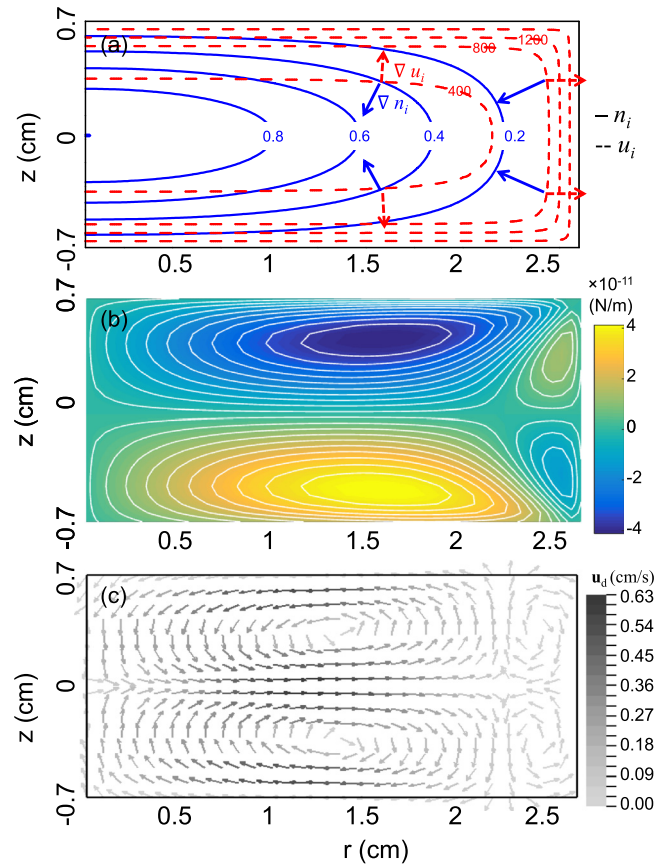

FIG. 2. (a) Contour plots of u_i (dashed lines) and n_i/n_{i0} (solid lines). (b) Contour plot of $(\nabla \times \mathbf{F})_\phi$. (c) Flow velocity $\mathbf{u}_d$ and obtained from numerical PDE solver.[25]

between the ambipolar electric field and the negatively charged dust particles and is given by $\mathbf{F}_{es} = -eZ_d\mathbf{E}$.[26] The electrostatic force on a single dust particle is curl-free because Eq. (5) shows that the ambipolar electric field $\mathbf{E} \sim \nabla(\ln n_i)$ and because ∇Z_d is nearly zero deduced from the facts that $Z_d \sim T_e \ln(T_e/T_i)$ when $\alpha \ll 1$ and that T_e and T_i are assumed to be uniform.

The thermophoretic force resulting from the spatial temperature gradient is given by[27]

$$\mathbf{F}_{th} = -\frac{32}{15}\frac{r_d^2}{v_{n,th}}\kappa_T \nabla T_n \left(1 + \frac{5\pi}{32}(1-\beta)\right), \tag{8}$$

where $v_{n,th}$ is the thermal speed of neutral gas molecules, κ_T is the thermal conductivity, and β is the thermal accommodation coefficient. Thus, the thermophoretic force is curl-free as is the gravitational force.

The ion drag force consists of two parts: (i) direct collisional impact of ions on dust particles and (ii) the long-range Coulomb interaction between ions and dust particles. Here, we consider only the ion drag force resulting from direct collisions as this dominates in the bulk plasma.[28] The ion drag force is then given by[29]

$$\mathbf{F}_{id} = \sigma_c n_i m_i v_i \mathbf{u}_i, \tag{9}$$

where σ_c is the dust grain effective cross-section and $v_i^2 = u_i^2 + v_{i,th}^2$. The effective dust grain collision cross-section σ_c can

be obtained from orbital motion-limited (OML) theory if the dust grain size is smaller than the ion Debye length and the ion mean free path is greater than the ion Debye length. With the measured nominal parameters, the ion mean free path is $\sim$100 μm and ion Debye length is $\sim$10 μm while the grain radius $<$10 μm (major radius is $\sim$9 μm and minor radius is $\sim$4.5 μm). OML theory is then applicable here and σ_c is given by[30]

$$\sigma_c = \pi r_d^2 \left(1 - \frac{2eV_d}{m_i v_i^2} \right), \tag{10}$$

where V_d is the dust grain floating potential. Because V_d is negative and large, σ_c greatly exceeds the geometric cross-section πr_d^2.

The ion drag force has a finite curl if ∇v_i and ∇n_i are not parallel as seen from the following argument that depends on the orbital motion enhancement of the cross-section. First, we observe that

$$\nabla \times \mathbf{F}_{id} = \nabla \times \left\{ \pi r_d^2 \left(1 - \frac{2eV_d}{m_i v_i^2} \right) n_i m_i v_i \mathbf{u}_i \right\}. \tag{11}$$

Since the ions are cold, $u_i \gg v_{i,th}$ and since $2e|V_d|/m_i u_i^2 \gg 1$, Eq. (11) can then be rewritten as

$$\nabla \times \mathbf{F}_{id} = -2eV_d \pi r_d^2 \nabla \times \left(\frac{n_i \mathbf{u}_i}{u_i} \right). \tag{12}$$

Because $\nabla \times \mathbf{u}_i = -\nabla \times (D_{a0}\nabla n_i/n_i) = 0$ and similarly $\nabla n_i \times \mathbf{u}_i = -\nabla n_i \times (D_{a0}\nabla n_i/n_i) = 0$, Eq. (12) reduces to

$$\nabla \times \mathbf{F}_{id} = -2eV_d \pi r_d^2 D_{a0} \frac{\nabla u_i}{u_i^2} \times \nabla n_i. \tag{13}$$

The contours of u_i and n_i/n_{i0} shown in Fig. 2(a) reveal that the gradient of u_i is not parallel to the gradient of n_i; the red dashed arrows indicate ∇u_i and the blue solid arrows indicate ∇n_i. Thus, the orbital motion enhancement of the effective dust grain cross-section causes the ion drag force on the dust grains to have a finite curl.

Numerical calculation of $\nabla \times \mathbf{F}_{id}$ obtained using $r_d = 10\,\mu$m, $V_d = -1.8$ V, and $n_i = 1.5 \times 10^{10}\,\text{cm}^{-3}$ reveals four separate quadrupole-like regions in the $\{r, z\}$ plane having finite curl as shown in Fig. 2(b). The negative (coming out of the plane) curls are shown in the inner upper and outer lower parts of the plasma while the positive (going into the plane) curls are seen in the inner lower and outer upper parts of the plasma.

The momentum equation of the dust fluid is

$$\left(\frac{\partial}{\partial t} + \mathbf{u}_d \cdot \nabla \right) \mathbf{u}_d = \frac{\mathbf{F}}{m_d} - \frac{\nabla P_d}{n_d m_d} + \nu_d \nabla^2 \mathbf{u}_d, \tag{14}$$

where ν_d is the kinematic viscosity of the dust particles. The poloidal velocity for an incompressible fluid has the form

$$\mathbf{u}_d = \frac{1}{2\pi} \nabla \Psi \times \nabla \phi, \tag{15}$$

where $\Psi(r, z)$ is the stream function through a circle of radius r at location z. Since $\mathbf{u}_d$ lies in the $\{r, z\}$ plane and the

system is axisymmetric, $\nabla \times \mathbf{u}_d$ is in the ϕ-direction. By employing a cylindrical vorticity, $\chi = r\hat{\phi} \cdot \nabla \times \mathbf{u}_d$ and by operating on Eq. (15) with $r^2\nabla\phi \cdot \nabla \times$ we obtain[31,32]

$$r^2 \nabla \cdot \left(\frac{1}{r^2} \nabla \Psi \right) = -2\pi\chi. \tag{16}$$

By using $\mathbf{u}_d \times \nabla \times \mathbf{u}_d = \frac{1}{2}\nabla(\mathbf{u}_d)^2 - \mathbf{u}_d \cdot \nabla\mathbf{u}_d$ and $\nabla \cdot \mathbf{u}_d = 0$ and by operating with $\nabla\phi \cdot \nabla \times$, Eq. (14) becomes[31,32]

$$\frac{\partial}{\partial t}\left(\frac{\chi}{r^2} \right) + \mathbf{u}_d \cdot \nabla\left(\frac{\chi}{r^2} \right) = \frac{1}{r}\frac{(\nabla \times \mathbf{F})_\phi}{m_d} + \nu_d \nabla \cdot \left(\frac{1}{r^2}\nabla\chi \right). \tag{17}$$

We solved Eqs. (15)–(17) numerically using FlexPDE.[25] The calculated $\mathbf{u}_d$ is shown in Fig. 2(c) which shows that counterclockwise vortices occur in the inner upper and the outer bottom plasma regions while clockwise vortices occur in the inner bottom and the outer upper regions. In the calculation, the four finite curl regions shown in Fig. 2(b) are modeled as Gaussian profiles, $\sim \exp(-r^2/\sigma_r^2 - z^2/\sigma_z^2)$. The inner curl regions are centered at $r = 1.2$ cm, $z = \pm 3.5$ mm with $\sigma_r = 0.54$ mm and $\sigma_z = 0.18$ mm; the outer curl regions are centered at $r = 2.4$ cm, $z = \pm 3.5$ mm with $\sigma_r = 0.18$ mm and $\sigma_z = 0.18$ mm; the peak values of the Gaussian function are obtained from Fig. 2(b). We assumed narrower FWHMs for the inner curl regions than what is shown in Fig. 2(b) because a dust-free region forms at the center of the plasma in the experiment. The center positions of the Gaussian function are shifted toward the $-r$ direction to minimize the boundary effect. The kinematic viscosity of the dust grains ν_d is known to be 10^{-2}–10^{-1} cm^{-2}/s (Ref. 3) and we assumed ν_d to be 10^{-1} cm^2/s. The boundary conditions we used are $u_r = 0$ at $r = 0$, $u_r = u_z = 0$ at the bottom and top electrodes and $\chi = \Psi = 0$ at the bottom and top electrodes.

III. EXPERIMENTAL RESULTS

Details of the Caltech ice dusty plasma experiment are described in Ref. 22. The plasma is ignited by applying 13.56 MHz rf across two disk electrodes separated by 1.4 cm and located in a small argon-filled vacuum chamber. The electrodes are cooled by liquid nitrogen, and the argon gas is cooled by being in contact with the electrodes. After a controlled amount of water vapor is injected directly into the chamber, water-ice grains spontaneously form and levitate between the two electrodes. The water-ice grains typically grow for 1–2 min and then stop growing. The final grain size and shape depend strongly on external conditions with larger and more elongated particles at lower ambient gas pressures[33] or in a plasma ignited with lighter gas.[23] Vortex flows start after grain growth stops.

An aluminum shroud (shown in Fig. 1(a) as gray squares) shields the electrodes and plasma from external thermal radiation to achieve a lower temperature. This heat shield lowers the temperatures of the top electrode from 135 K to 130 K and the temperature of the bottom electrode from 165 K to 130 K. This shielding was essential for obtaining plasmas having high symmetry about the $z = 0$ midplane. A He-Ne laser sheet projected through a vacuum chamber side window illuminates a poloidal cross-section of the ice grain vortex flow. Sequential

images of the illuminated grains are obtained by a digital SLR camera having a telescopic lens and a filter transmitting only the He-Ne laser light. The exposure time is 1/60 s, and the frame rate is 60 fps.

A typical dust particle vortex flow is shown in Fig. 3(a) (Multimedia view); the print image in Fig. 3(a) is the superposition of 10 sequential images from a video file which appears by clicking the URL provided in the caption of Fig. 3(a). Note that the print image in Fig. 3(a) only shows the right side of plasma whereas the video file obtained by clicking the URL in the caption of Fig. 3(a) shows the entire plasma region (both left and right of z axis). The flow vector field in the yellow box in Fig. 3(a) is determined by particle image velocimetry[34] and shown as arrows in Fig. 3(b). The curl of the dust flow velocity, $\nabla \times \mathbf{u}_d$, calculated from the vector field is shown in Fig. 3(b) as a color map and reveals negative curl in the upper-inner and lower-outer regions. It also reveals positive curl in the lower-outer and upper-inner regions; this anti-symmetry is consistent with Figs. 2(b) and 2(c).

The plasma was ignited at 200 mTorr Ar pressure using 2 W rf power; a Langmuir probe measurement indicated that $n_i = 1.5 \times 10^{10} \, \mathrm{cm}^{-3}$. Close-up images obtained using a long distance microscope lens show that the ice grains are not spherical and have a 18 μm length and a 9 μm width.[33] The fact that four axisymmetric vortex toroids appear in Fig. 3(b) as predicted in Figs. 2(b) and 2(c) indicate that the 2:1 grain elongation does not affect the validity of the model. The outer region vortices are less distinct than the inner region vortices because the camera field of view is partially blocked by the heat shield. The vortex flow direction agrees with the model; counterclockwise for the inner upper and outer lower toroids and clockwise for the inner lower and outer upper toroids (see colors representing curl in Fig. 3(b)). Furthermore, the
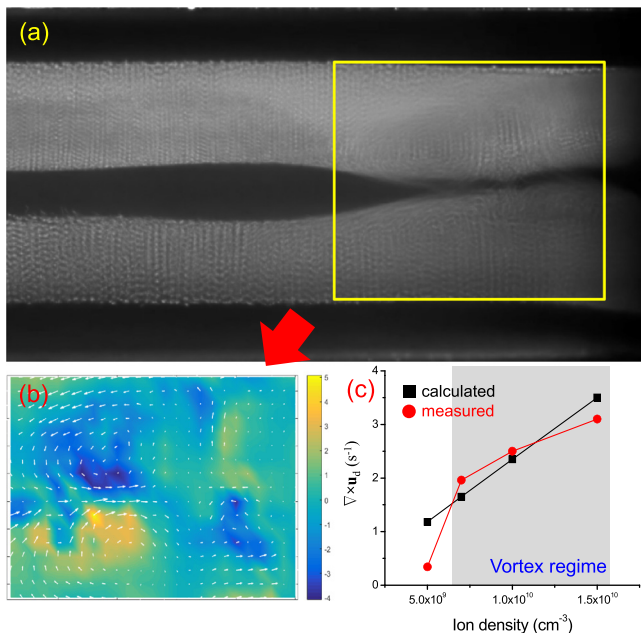
observed ice grain flow velocity in the vortex is a few mm/s which is the order of magnitude of the numerical calculation prediction. Besides the agreement between experimental and numerical results, an additional observation supports the presumption that a finite curl of the ion drag force causes the vortex flows; measured $\nabla \times \mathbf{u}_d$ increases as the ion density increases above the critical density as seen in Fig. 3(c). This trend is also seen in Eq. (13); since $\mathbf{u}_i = -(D_{a0} \nabla n_i / n_i)$, $\nabla \times \mathbf{F}_{id} \sim n_i / L$.

It is also observed that the closed vortex motion appears only when the plasma density exceeds a critical value (here, $n_i > 5 \times 10^9 \, \mathrm{cm}^{-3}$). We do not know what prevents the dust grains from whirling at the low ion density but the neutral gas friction could be a possible candidate.

Figure 4(a) (Multimedia view) shows that a different situation occurs when the aluminum heat shield is removed; the print image in Fig. 4(a) is the superposition of 10 sequential images from a video file which appears by clicking the URL in the caption of Fig. 4(a) and the print image shows the right side of plasma only whereas the video file shows the entire plasma region (both left and right of z axis). Now, unlike Fig. 3(a) there are only two vortex toroids and the flow direction is counterclockwise for *both* vortex toroids as sketched in Fig. 1(b). Except for the removal of the heat shield, all other external parameters are identical to those used for Fig. 3(a). It is again observed that $\nabla \times \mathbf{u}_d$ increases as the ion density of plasma increases, suggesting that ion drag force is also the cause of the observed co-rotating vortex flows. Based on this observation and the fact that the top electrode is 30 K cooler than the bottom electrode when the heat shield is removed, the observed co-rotating vortices can be explained as follows: Removal of the heat shield causes development of strong neutral (∇T_n) and ion temperature

FIG. 3. (a) Vortex motion captured in Ar plasma with heat shield (Multimedia view) [URL: http://dx.doi.org/10.1063/1.4941973.1]. (b) Flow vector field (arrows) obtained from particle image velocimetry[34] and $\nabla \times \mathbf{u}_d$ (color map) (c) Calculated and measured $\nabla \times \mathbf{u}_d$ as a function of ion density.
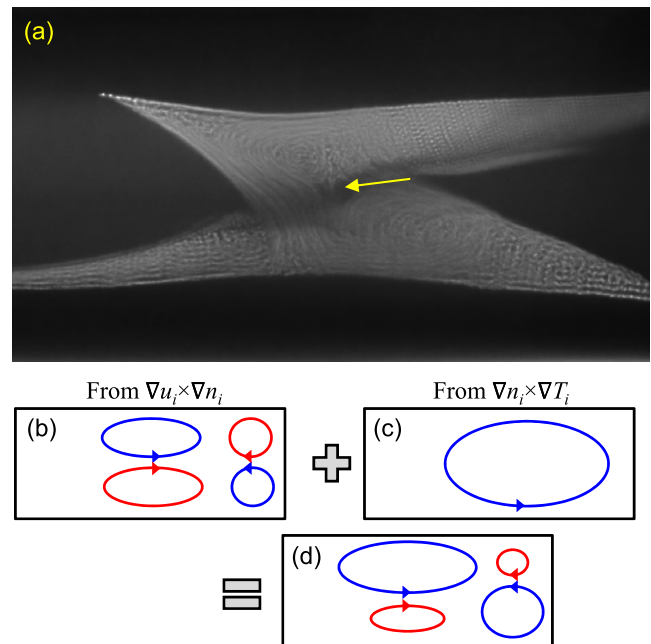

FIG. 4. (a) Vortex motion captured in Ar plasma having no heat shield. Sketches of $\nabla \times \mathbf{F}_{id}$ from two components (Multimedia view) [URL: http://dx.doi.org/10.1063/1.4941973.2]. (b) $\nabla u_i \times \nabla n_i$, and (c) $\nabla n_i \times \nabla T_i$, and (d) the summation of two.

gradients (∇T_i) in the negative z-direction. The curl of the pressure term in the ion momentum equation is $-\nabla \times (\nabla P_i/n_i m_i) = -\nabla \times \{\nabla(n_i k_B T_i)/n_i m_i\} = -k_B \nabla T_i \times \nabla n_i / n_i m_i$ and so is finite when ∇T_i is finite. Since ∇T_i is not parallel to ∇n_i, a single large counterclockwise ion vortex flow is developed making $\nabla \times \mathbf{u}_i$ finite and negative (blue) as sketched in Fig. 4(c). If we consider this finite $\nabla \times \mathbf{u}_i$ in Eq. (12) when calculating $\nabla \times \mathbf{F}_{id}$, the negative (blue) curls shown in the inner upper and outer lower regions of Fig. 4(b) become enhanced while the positive (red) curls in the inner lower and outer upper regions become diminished, so the negative (blue) vortices become dominant. This leads to the co-rotating, radially offset toroids seen in Fig. 4(a) (Multimedia view) and sketched in Fig. 4(d).

IV. ANALOGY TO POLOIDAL MAGNETIC FIELD

Since $\mathbf{u}_d$, χ, and Ψ are mathematically equivalent to poloidal magnetic field $\mathbf{B}$, $\mu_0 J_\phi/r$, and poloidal magnetic flux ψ, respectively, the vortex flows are analogs to poloidal magnetic fields. Thus, the interface between the two co-rotating vortices in Fig. 4(a) (Multimedia view) has a structure analogous to magnetic reconnection. Just as two oppositely directed magnetic fields reconnect at the interface between two same-sense poloidal fields having different magnetic axes, two opposite flows exist at the interface between two co-rotating vortex toroids. Just as in a magnetic reconnection situation, an X-point between the two vortex toroids is seen in Fig. 4(a) (Multimedia view), indicated by an arrow (this X-point is seen much more clearly in the video file obtained by clicking the URL provided in the caption of Fig. 4(a)). In magnetic reconnection governed by resistive MHD, the Lundquist number $S = v_A L'/(\eta/\mu_0)$ is related to the reconnection layer width δ by the relation $\delta = L'/S^{1/2}$ where L' is the reconnection layer length. From Fig. 4(a) (Multimedia view), it is seen that $\delta = 0.5$ mm and $L' = 1$ mm implying that if this were a magnetic reconnection the Lundquist number would be $S = 4$. The dusty plasma quantity corresponding to S is the Reynolds number, $R_e = UL''/\nu_d$ where U is the characteristic velocity and L'' is the characteristic size. Assuming $L'' \simeq 0.3$ cm, $U \simeq 0.2 - 1$ cm/s, and $\nu_d = 10^{-1} - 10^{-2}$ cm^{-2}/s we obtain $0.6 < R_e < 30$ which is consistent with observed X-point geometry. The dusty plasma experiment thus offers a highly visual analog of resistive MHD magnetic reconnection.

V. ESTIMATION OF α

We now validate the assumption that $\alpha = Z_d n_d/n_i$ in our experiment is small. The ice grain number density n_d is determined from direct measurement of the intergrain distance a in a single movie frame. The measured distance is $a = 280\,\mu$m which gives $n_d = a^{-3} = 4.6 \times 10^4$ cm^{-3}. The ion density n_i measured by a Langmuir probe is $5 \times 10^9 - 1.5 \times 10^{10}$ cm^{-3}. Since the dust charge potential V_d is approximately $T_e \simeq 2$ eV and since the nominal observed grain radius is $4.5\,\mu$m $< r_d < 9\,\mu$m, the dust charge number is $Z_d \simeq 4\pi\varepsilon_0 r_d T_e/e \simeq 6 \times 10^3 - 12 \times 10^3$ assuming the grains are nominally spherical. We then obtain $0.02 < \alpha < 0.11$ which is indeed small.

[1]H. Thomas, G. E. Morfill, V. Demmel, J. Goree, B. Feuerbacher, and D. Mohlmann, Phys. Rev. Lett. **73**, 652 (1994).
[2]H. M. Thomas and G. E. Morfill, Nature **379**, 806 (1996).
[3]G. E. Morfill, M. Rubin-Zuzic, H. Rothermel, A. V. Ivlev, B. A. Klumov, H. M. Thomas, U. Konopka, and V. Steinberg, Phys. Rev. Lett. **92**, 175004 (2004).
[4]Y. Feng, J. Goree, and B. Liu, Phys. Rev. Lett. **109**, 185002 (2012).
[5]R. Heidemann, S. Zhdanov, K. R. Suetterlin, H. M. Thomas, and G. E. Morfill, Europhys. Lett. **96**, 15001 (2011).
[6]M. Schwabe, S. Zhdanov, C. Rath, D. B. Graves, H. M. Thomas, and G. E. Morfill, Phys. Rev. Lett. **112**, 115002 (2014).
[7]G. E. Morfill, H. M. Thomas, U. Konopka, H. Rothermel, M. Zuzic, A. Ivlev, and J. Goree, Phys. Rev. Lett. **83**, 1598 (1999).
[8]O. S. Vaulina, A. P. Nefedov, O. F. Petrov, and V. E. Fortov, J. Exp. Theor. Phys. **91**, 1147 (2000).
[9]M. Rubin-Zuzic, H. M. Thomas, S. K. Zhdanov, and G. E. Morfill, New J. Phys. **9**, 39 (2007).
[10]S. Shimizu, B. Klumov, T. Shimizu, H. Rothermel, O. Havnes, H. M. Thomas, and G. E. Morfill, J. Geophys. Res.: Atmos. **115**, D18205 (2010).
[11]D. A. Law, W. H. Steel, B. M. Annaratone, and J. E. Allen, Phys. Rev. Lett. **80**, 4189 (1998).
[12]M. Klindworth, A. Melzer, A. Piel, and V. A. Schweigert, Phys. Rev. B **61**, 8404 (2000).
[13]M. R. Akdim and W. J. Goedheer, Phys. Rev. E **67**, 056405 (2003).
[14]M. Schwabe and D. B. Graves, Phys. Rev. E **88**, 023101 (2013).
[15]V. E. Fortov, O. S. Vaulina, O. F. Petrov, V. I. Molotkov, A. V. Chernyshev, A. M. Lipaev, G. Morfill, H. Thomas, H. Rotermell, S. A. Khrapak et al., J. Exp. Theor. Phys. **96**, 704 (2003).
[16]J. Wesson, Tokamaks, 4th ed. (Oxford University Press, Oxford, UK, 2011).
[17]P. M. Bellan, Spheromaks: A Practical Application of Magnetohydrodynamic Dynamos and Plasma Self-Organization (Imperial College Press, London, 2000).
[18]E. N. Parker, J. Geophys. Res. **62**, 509, doi:10.1029/JZ062i004p00509 (1957).
[19]P. A. Sweet, in Electromagnetic Phenomena in Cosmical Physics, edited by B. Lehnert (Cambridge University Press, 1958).
[20]X. H. Deng and H. Matsumoto, Nature **410**, 557 (2001).
[21]Y. Ono, H. Tanabe, Y. Hayashi, T. Ii, Y. Narushima, T. Yamada, M. Inomoto, and C. Z. Cheng, Phys. Rev. Lett. **107**, 185001 (2011).
[22]K. B. Chai and P. M. Bellan, Geophys. Res. Lett. **40**, 6258, doi:10.1002/2013GL058268 (2013).
[23]K. B. Chai and P. M. Bellan, Astrophys. J. **802**, 112 (2015).
[24]M. A. Lieberman and A. J. Lichtenber, Principles of Plasma Discharges and Materials Processing, 2nd ed. (John Wiley and Sons, Inc., Hoboken, New Jersey, USA, 2005).
[25]See http://www.pdesolutions.com/index.html for PDE Solutions Inc., FlexPDE^{TM}.
[26]J. E. Daugherty, R. K. Porteous, and D. B. Graves, J. Appl. Phys. **73**, 1617 (1993).
[27]L. Talbot, R. K. Cheng, R. W. Schefer, and D. R. Willis, J. Fluid Mech. **101**, 737 (1980).
[28]A. Bouchoule, Dusty Plasmas: Physics, Chemistry, and Technological Impact in Plasma Processing (John Wiley and Sons, Inc., Chichester, England, UK, 1999).
[29]M. S. Barnes, J. H. Keller, J. C. Forster, J. A. ONeill, and D. K. Coultas, Phys. Rev. Lett. **68**, 313 (1992).
[30]I. B. Bernstein and I. N. Rabinowitz, Phys. Fluids **2**, 112 (1959).
[31]P. M. Bellan, Phys. Rev. Lett. **69**, 3515 (1992).
[32]P. M. Bellan, Fundamentals of Plasma Physics (Cambridge University Press, Cambridge, UK, 2006).
[33]K. B. Chai and P. M. Bellan, J. Atmos. Sol.-Terr. Phys. **127**, 83 (2015).
[34]A. Liberzon, R. Gurka, and Z. Taylor, see http://www.openpiv.net for OpenPIV home page, 2009.